JOURNAL OF THE MECHANICAL BEHAVIOR OF BIOMEDICAL MATERIALS 4 (2011) 1167–1176

available at www.sciencedirect.com

journal homepage: www.elsevier.com/locate/jmbbm

Research paper

Active contraction of cardiac muscle: In vivo characterization of mechanical activation sequences in the beating heart

Alkiviadis Tsamis[a], *Wolfgang Bothe*[b], *John-Peder Escobar Kvitting*[b], *Julia C. Swanson*[b], *D. Craig Miller*[b], *Ellen Kuhl*[a,b,c,*]

[a] *Department of Mechanical Engineering, 496 Lomita Mall, Stanford, CA-94305, USA*
[b] *Department of Cardiothoracic Surgery, 300 Pasteur Drive, Stanford, CA-94305, USA*
[c] *Department of Bioengineering, 496 Lomita Mall, Stanford, CA-94305, USA*

ARTICLE INFO

Article history:
Received 22 January 2011
Received in revised form
22 March 2011
Accepted 29 March 2011
Published online 7 April 2011

Keywords:
Biomechanics
Cardiac mechanics
Muscle
Excitation
Contraction
Transmural strains

ABSTRACT

Progressive alterations in cardiac wall strains are a classic hallmark of chronic heart failure. Accordingly, the objectives of this study are to establish a baseline characterization of cardiac strains throughout the cardiac cycle, to quantify temporal, regional, and transmural variations of active fiber contraction, and to identify pathways of mechanical activation in the healthy beating heart. To this end, we insert two sets of twelve radiopaque beads into the heart muscle of nine sheep; one in the anterior-basal and one in the lateral-equatorial left ventricular wall. During three consecutive heartbeats, we record the bead coordinates via biplane videofluoroscopy. From the resulting four-dimensional data sets, we calculate the temporally and transmurally varying Green–Lagrange strains in the anterior and lateral wall. To quantify active contraction, we project the strains onto the local muscle fiber directions. We observe that mechanical activation is initiated at the endocardium slightly after end diastole and progresses transmurally outward, reaching the epicardium slightly before end systole. Accordingly, fibers near the outer wall are in contraction for approximately half of the cardiac cycle while fibers near the inner wall are in contraction almost throughout the entire cardiac cycle. In summary, cardiac wall strains display significant temporal, regional, and transmural variations. Quantifying wall strain profiles might be of particular clinical significance when characterizing stages of left ventricular remodeling, but also of engineering relevance when designing new biomaterials of similar structure and function.

1. Introduction

Repairing the failing heart is a desirable but elusive goal. Despite tremendous scientific progress during the past decades, heart failure remains one of the most common, costly, disabling, and deadly medical conditions affecting more than 25 million people worldwide (Lloyd-Jones et al., 2010). Dilation of the left ventricle, change in ventricular shape, and

* *Corresponding author at:* Department of Mechanical Engineering, 496 Lomita Mall, Stanford, CA-94305, USA. Tel.: +1 650 450 0855; fax: +1 650 725 1587.
E-mail address: ekuhl@stanford.edu (E. Kuhl).
URL: http://biomechanics.stanford.edu (E. Kuhl).

1751-6161/$ - see front matter © 2011 Elsevier Ltd. All rights reserved.
doi:10.1016/j.jmbbm.2011.03.027

decrease in ejection fraction are clinical indicators of disease progression and strong predictors of survival (Gaudron et al., 1993). Effective therapies for heart failure seek to attenuate these effects and reverse disease progression (McGee et al., 2006). Particularly promising examples are biomaterial approaches that seek to support the ventricular wall to reduce stress and alleviate cardiomyocyte overstretch (Christman and Lee, 2006). Research in biomaterials currently focuses on three mechanisms of wall support: The injection of living cells into the myocardium to create in situ engineered cardiac tissue (Wollert et al., 2004); the implantation of in vitro engineered tissue patches (Böl et al., 2009; Leong et al., 2008); and the implantation of synthetic patches or passive cardiac support devices around the heart (Cheng et al., 2006b). The objective of this study is to provide guidelines for the structural and functional requirements of these biomaterial solutions. In particular, we seek to establish a baseline characterization of cardiac and fiber strains throughout the cardiac cycle, to quantify temporal, regional, and transmural variations of active muscle contraction, and to identify pathways of mechanical activation in the healthy beating heart. This baseline characterization of cardiac strains is also of clinical significance since it may help to judge strain alterations in response to cardiac disease.

For more than 30 years, the use of implanted radiopaque markers has provided considerable insight into the complex transmural dynamics of the healthy and diseased ventricular myocardium. In the first series of experiments, small lead spheres were inserted with a needle into the anterior left ventricular wall of five canine hearts to characterize the complex transmural deformation pattern using biplane cineradiography (Fenton et al., 1978). Ventricular wall strains were extracted from the experimentally measured marker coordinates using the field theories of continuum mechanics. While the data analysis was initially based on the assumption of infinitesimal deformations, subsequent studies demonstrated the need to extend the analysis to finite deformations (Waldman et al., 1985). Over the years, the bead insertion technique was refined and standardized to the method we have adopted within this study (Cheng et al., 2005a; Waldman et al., 1985). One of the major breakthroughs enabled by the transmural marker technique was to precisely quantify how individual strain components change with depth, from the epicardium, the outer wall, to the endocardium, the inner wall. While the earlier studies used a discrete point-wise representation of strains, refined methods now use a continuous functional representation, either in the form of fitted bilinear cubic finite elements (McCulloch and Omens, 1991) or fitted polynomials (Kindberg et al., 2007), the method we adopt here. In combination with tissue histology, this functional representation naturally lends itself to the quantification of fiber and sheet strains which have significantly improved our understanding of the mechanics underlying coordinated pump function (Arts et al., 2001; Cheng et al., 2005b, 2008; Costa et al., 1999).

Throughout the past two decades, marker-based strain characterization has been used both in canine (Arts et al., 2001; Costa et al., 1999; McCulloch and Omens, 1991; Waldman et al., 1985) and ovine (Carhäll et al., 2008; Cheng et al., 2005a,b, 2006a; Kindberg et al., 2007) hearts, with generally similar results, however, strains being slightly larger in dogs than in sheep. The marker technique has been used successfully to identify the impact of acute changes in strain profiles, for example initiated by varying afterload (Takayama et al., 2002) or by ventricular pacing (Coppola et al., 2007). However, the true beauty of this technique lies in its permanent nature allowing to precisely quantify chronic changes, for example in response to mitral regurgitation (Carhäll et al., 2008) or myocardial infarction, in its plain form, or treated with a passive support device (Cheng et al., 2006a). Overall, this technique is relatively well-known in the surgical community but less so in the engineering community. One of the goals of this manuscript is therefore to discuss this technique in view of a modern continuum mechanics analysis which allows us to reconstruct the tensorial characterization of ventricular wall kinematics.

Most existing marker studies use the end-diastolic state as the reference configuration and the end-systolic state as the deformed configuration. Accordingly, they fail to give a complete picture of the spatio-temporal strain evolution across the ventricular wall. Using a novel time-aligned averaging technique to create a functional representation of the underlying Green–Lagrange strains (Rausch et al., 2011, in press), we reconstruct strain profiles throughout the entire wall throughout the entire cardiac cycle averaged over nine animals. This allows us to visualize the mechanical activation sequence across the ventricular wall. The resulting color-coded graphics demonstrate that maximum fiber contraction may in fact occur significantly after the end-systolic state.

2. Materials and methods

We premedicate nine adult male dorsett-hybrid sheep with ketamine, anesthesize them with sodium thiopental, intubate and ventilate them, and maintained general anesthesia with inhalational isoflurane and supplemental oxygen. After performing a left thoracotomy, we measure the wall thickness at the anterior-basal and at the lateral-equatorial regions of the left ventricular wall using epicardial echocardiography. At each of these two regions, we insert three transmural columns of four bead sets each (Waldman et al., 1985); see Fig. 1. Using a depth-adjustable bead insertion trocar, we first insert three 0.7 mm diameter beads in each column, evenly spaced between the endo- and epicardial surfaces. In addition, we sew a fourth 1.7 mm diameter bead onto the epicardial surface above each column. To access the left ventricular volume, we implant thirteen evenly spaced epicardial markers silhouetting the left ventricle. Before taking the animals to the catheterization laboratory for data acquisition, we place an implantable micromanometer pressure transducer in the left ventricular chamber and a micromanometer catheter into the ascending aorta for ventricular and aortic pressure measurements. During baseline conditions with the heart in normal sinus rhythm and the animals in the right lateral decubitus position, we record videofluoroscopic images of all beads and markers using biplane videofluoroscopy at a sampling frequency of 60 Hz. We simultaneously record aortic pressure, left ventricular pressure, and electrocardiogram voltage signals.

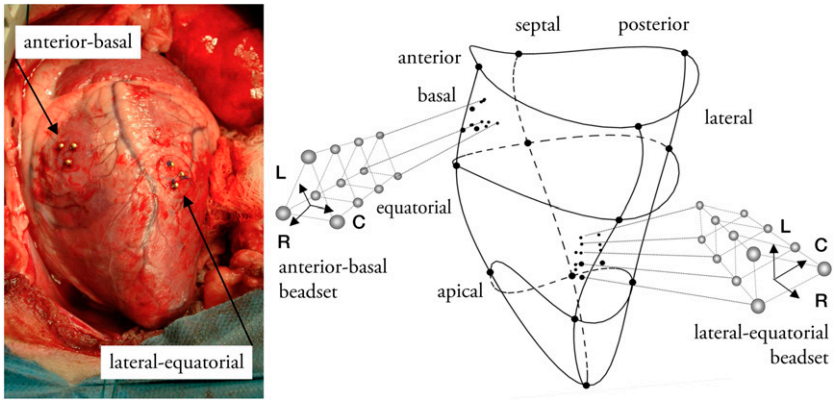

Fig. 1 – Locations of transmural beadsets in the anterior-basal and lateral-equatorial left ventricular wall, left. Left ventricle with both beadsets silhouetted by thirteen epicardial markers, right. C, R, and L denote the axes of the local circumferential–radial–longitudinal coordinate system.

Using a semi-automated image processing and digitization software developed in our laboratory (Niczyporuk and Miller, 1991), we obtain three-dimensional coordinates $\mathbf{x}(\boldsymbol{X}, t)$ of the four by three beads of both bead sets and of the thirteen left ventricular markers offline from the acquired biplane images. The accuracy of our three-dimensional displacement reconstruction from biplane videofluoroscopy is 0.1 ± 0.3 mm (Daughters et al., 1989).

3. Theory and calculation

3.1. *Cardiac coordinates*

To create a functional representation of the strain field in the anterior-basal and lateral-equatorial wall, we define a local Cartesian coordinate system $\{\boldsymbol{e}_c, \boldsymbol{e}_l, \boldsymbol{e}_r\}$ aligned with the local circumferential, radial, and longitudinal directions; see Fig. 1. We place its origin into the geometric center of three epicardial beads which define a plane tangential to the outer cardiac wall. The radial axis $\boldsymbol{e}_r$ is oriented normal to this tangential plane, with a positive outward direction. The circumferential axis $\boldsymbol{e}_c$ is introduced normal to the vector connecting the apex of the heart with the origin of the coordinate system and normal to the radial axis, pointing in the mathematically positive direction when viewing the heart from base to apex. The longitudinal axis $\boldsymbol{e}_l$ is defined normal to the radial and circumferential axes, $\boldsymbol{e}_l = \boldsymbol{e}_r \times \boldsymbol{e}_c$, with a positive direction from apex to base; see Fig. 1.

3.2. *Temporal interpolation and data analysis*

To create an average strain representation in the anterior-basal and lateral-equatorial wall, we map all nine experimental data sets into four time intervals between End Diastole, ED, End Isovolumic Contraction, EIC, End Systole, ES, and End Isovolumic Relaxation, EIR, as previously described (Rausch et al., 2011, in press). We select these characteristic time points semi-manually from the individual pressure–volume relationships, with the volume defined in terms of the thirteen silhouetting epicardial markers. Based on different average interval lengths, these four time intervals are further subdivided into five segments from ED to EIC, eleven segments from EIC to ES, seven segments from ES to EIR, and ten segments from EIR to ED, respectively. Within each of these four intervals, we perform a linear temporal interpolation between the experimentally acquired raw data points $\mathbf{x}(\boldsymbol{X}, t)$ to create temporally aligned data sets of hemodynamic and kinematic data at the corresponding five, eleven, seven, and ten segment points, thus representing the cardiac cycle through t_n discrete time points with $n = 1, \ldots, 33$. Using these time-aligned data sets, we perform the strain calculations described in the following section to extract the means and standard deviations of the Green–Lagrange strain components $\boldsymbol{E}(\boldsymbol{X}, t)$ and fiber strains $E_{FF}(\boldsymbol{X}, t)$ at 33 discrete time points throughout the cardiac cycle.

3.3. *Spatial interpolation and cardiac strains*

We assume that within the space enclosed by each bead set, the current placement $\boldsymbol{\varphi}(\boldsymbol{X}, t)$ of each material point $\boldsymbol{X}$ at each time t can be approximated by a time-dependent mapping $\mathbf{c}_I(t)$ of the spatial interpolation $N_I(\boldsymbol{X})$ in the reference configuration,

$$\boldsymbol{\varphi}(\boldsymbol{X}, t) = \sum_{I=1}^{n_{apx}} \mathbf{c}_I(t) N_I(\boldsymbol{X}) \tag{1}$$

where $I = 1, \ldots, n_{apx}$ is the order of the approximation. In particular, at each of the $J = 1, \ldots, n_{pnt}$ experimentally measured data points with $n_{pnt} = 12$, this implies that

$$\mathbf{x}_J(t) = \sum_{I=1}^{n_{apx}} \mathbf{c}_I(t) N_I(\boldsymbol{X}_J) \tag{2}$$

where $\mathbf{x} = [x_c, x_l, x_r]^t$ are the measured data points, $\mathbf{c} = [c_c, c_l, c_r]^t$ are the unknown coefficients at each discrete time point t associated with the circumferential, longitudinal, and radial directions, and N_I are the interpolation terms associated with the corresponding coordinates $\boldsymbol{X}$ of point J in the reference configuration, in our case, at end diastole. Following the literature (Kindberg et al., 2007), we choose a

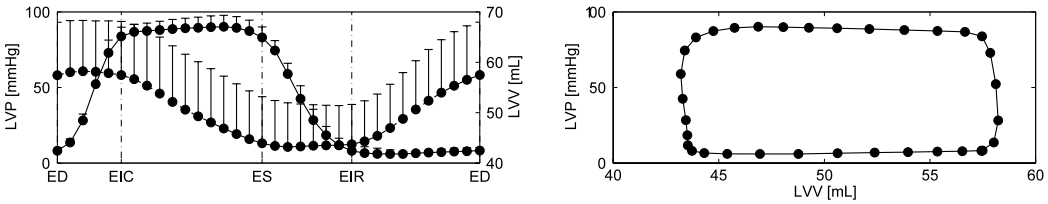

Fig. 2 – Temporal evolution of left ventricular pressure and volume, left, and average pressure–volume loop, right. The left ventricular pressure exhibits the characteristic n-shape with small standard deviations. The left ventricular volume varies between 57.4 ± 10.5 mL at ED and 43.9 ± 9.3 mL at ES. Average stroke volume and average ejection fraction are 15 mL and 26%, respectively. Means and standard deviations are displayed for $n = 9$ animals to the top of the curve. LVP left ventricular pressure, LVV left ventricular volume, ED end diastole, EIR end isovolumetric relaxation, ES end systole, and EIC end isovolumetric contraction.

linear interpolation in the circumferential and longitudinal directions and a quadratic interpolation in the radial direction such that N_I can be expressed through the following $n_{apx} = 9$ terms, $N_I = [X_c X_r^2, X_c X_r, X_c, X_l X_r^2, X_l X_r, X_l, X_r^2, X_r, 1]^t$. Since we acquire the coordinates of twelve data points while only applying an approximation with nine unknowns, i.e., $n_{pnt} = 12 > n_{apx} = 9$, the overall system for the unknown coefficients $\mathbf{c}_I$

$$\mathbf{x}(t)_{[3\times12]} = \mathbf{c}(t)_{[3\times9]} \cdot \mathbf{N}_{[9\times12]} \tag{3}$$

is overdetermined. In the above matrix representation of Eq. (2), we have introduced the matrix notation for the measured coordinates of the data points $\mathbf{x}_{[3\times12]} = [\boldsymbol{x}_1, \ldots, \boldsymbol{x}_{12}]$, for the unknown coefficients $\mathbf{c}_{[3\times9]} = [\mathbf{c}_1, \ldots, \mathbf{c}_9]$, and for the interpolation matrix $\mathbf{N}_{[9\times12]} = [N_I(\mathbf{X}_1), \ldots, N_I(\mathbf{X}_{12})]^t$. We solve this system for the unknown coefficient matrix $\mathbf{c}(t)$ using the pseudo inverse of the interpolation matrix $\mathbf{N}$.

$$\mathbf{c}(t)_{[3\times9]} = \mathbf{x}(t)_{[3\times12]} \cdot \mathbf{N}^t_{[12\times9]} \cdot [\mathbf{N}_{[9\times12]} \cdot \mathbf{N}^t_{[12\times9]}]^{-1}. \tag{4}$$

With the coefficients $\mathbf{c}(t)$ known at each discrete time point t, we can evaluate the nonlinear deformation map $\boldsymbol{\varphi}(\mathbf{X}, t) = \sum_{I=1}^{n_{apx}} \mathbf{c}_I(t) N_I(\mathbf{X})$ as introduced in Eq. (1). Accordingly, the deformation gradient $\boldsymbol{F} = \nabla\boldsymbol{\varphi}$ takes the following functional representation,

$$\boldsymbol{F}(\mathbf{X}, t) = \sum_{I=1}^{n_{apx}} \mathbf{c}_I(t) \otimes \nabla N_I(\mathbf{X}) \tag{5}$$

where $\nabla(\circ) = [\partial_c(\circ), \partial_l(\circ), \partial_r(\circ)]^t$ denotes the spatial gradient with respect to the local cardiac coordinate system. The Green–Lagrange strain tensor in the cardiac coordinate system can then be expressed as follows.

$$\boldsymbol{E}(\mathbf{X}, t) = \frac{1}{2}[\boldsymbol{F}^t \cdot \boldsymbol{F} - \boldsymbol{I}]. \tag{6}$$

Using regionally and transmurally varying fiber directions reported in the literature (Ennis et al., 2008), we project the Green–Lagrange strain tensor onto the local fiber direction $\boldsymbol{f}(\mathbf{X})$

$$\mathrm{E}_{\mathrm{FF}}(\mathbf{X}, t) = \boldsymbol{f}(\mathbf{X}) \cdot \boldsymbol{E}(\mathbf{X}, t) \cdot \boldsymbol{f}(\mathbf{X}) \tag{7}$$

to characterize the local fiber strains $\mathrm{E}_{\mathrm{FF}}(\mathbf{X}, t)$. To illustrate the transmural variation of the cardiac strains and fiber strains, we evaluate Eqs. (6) and (7) for varying depths, i.e., along the radial direction $\boldsymbol{X} = [0, 0, X_r]^t$.

4. Results

4.1. *Hemodynamics*

Fig. 2 shows the temporal evolution of the averaged left ventricular pressure LVP and left ventricular volume LVV over the cardiac cycle, left, and the resulting averaged pressure–volume loop, right. The left ventricular pressure exhibits the characteristic n-shape with small standard deviations. The left ventricular volume remains virtually unchanged during isovolumetric contraction from ED to EIC, with an end-diastolic volume of 57.4 ± 10.5 mL. It decreases during ejection from EIC to ES, reaching an end-systolic volume of 43.9 ± 9.3 mL. Average stroke volume and average ejection fraction are 15 mL and 26%, respectively. With average end-systolic and end-diastolic pressures of 83.1 ± 7.0 mmHg and 8.1 ± 2.2 mmHg, the average cardiac energy production per beat is 0.15 J, corresponding to the area enclosed by the pressure–volume loop.

4.2. *Spatio-temporal evolution of cardiac strains in the anterior wall*

Fig. 3 summarizes the temporal evolution of the average cardiac strains in the anterior-basal left ventricular midwall, i.e., at 50% depth, at which the fiber direction is approximately aligned with the circumferential direction. The circumferential strains E_{CC} displayed on the top left are slightly tensile after end diastole with a maximum value of +2.0 ± 1.7% at end isovolumetric contraction, then become compressive and decrease towards their minimum value of −7.9 ± 3.8% at end isovolumetric relaxation, before returning back to zero at end diastole. The radial strains E_{RR} displayed on the bottom left behave in the opposite way. The wall thins slightly from end diastole towards −3.8±3.5% at end isovolumetric contraction, then thickens during systole towards +11.3 ± 6.4% at end isovolumetric relaxation, before returning back to zero at end diastole.

Fig. 4 displays the spatio-temporal evolution of the average cardiac strains across the anterior-basal left ventricular wall over three consecutive beats, where red indicates positive, i.e., tensile strains, and blue indicates negative, i.e., compressive strains. Mechanical activation characterized through the transition from red to blue in the circumferential strain E_{CC} begins at the endocardium, the inner wall, at

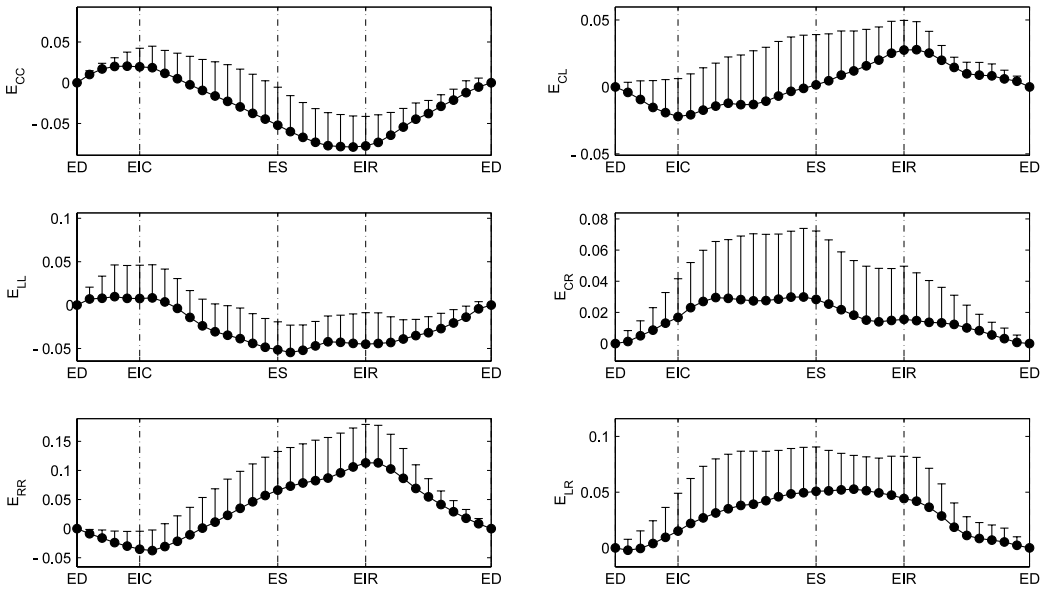

Fig. 3 – Temporal evolution of cardiac strains at 50% depth of the anterior-basal left ventricular wall. Maximum circumferential contraction E_{CC} is $-7.9 \pm 3.8\%$ and maximum wall thickening E_{RR} is $+11.3 \pm 6.4\%$. Means and standard deviations of components of the Green–Lagrange strains are displayed for $n = 9$ animals to the top of the curves. C circumferential, R radial, and L longitudinal direction. ED end diastole, EIR end isovolumetric relaxation, ES end systole, and EIC end isovolumetric contraction.

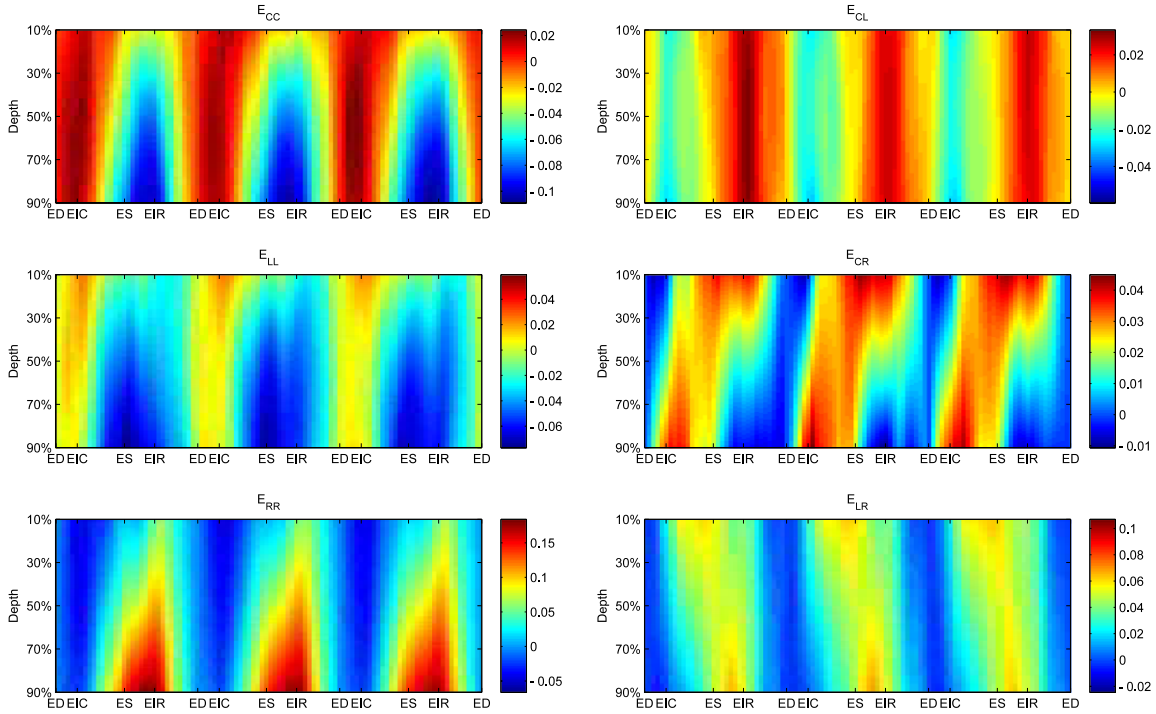

Fig. 4 – Spatio-temporal evolution of cardiac strains in the anterior-basal left ventricular wall averaged over $n = 9$ animals. Components of the Green–Lagrange strains are displayed across the ventricular wall with 10% depth indicating the epicardium, the outer wall, and 90% depth indicating the endocardium, the inner wall. Strains are displayed for three consecutive heartbeats. C circumferential, R radial, and L longitudinal direction. ED end diastole, EIR end isovolumetric relaxation, ES end systole, and EIC end isovolumetric contraction.

90% depth, and then progresses towards the epicardium, the outer wall, at 10% depth. Mechanical deactivation, however, progresses vice versa, beginning at the epicardium and progressing towards the endocardium. This implies that the cells that are *activated first* are *deactivated last*. Mechanical deactivation proceeds faster than mechanical activation as

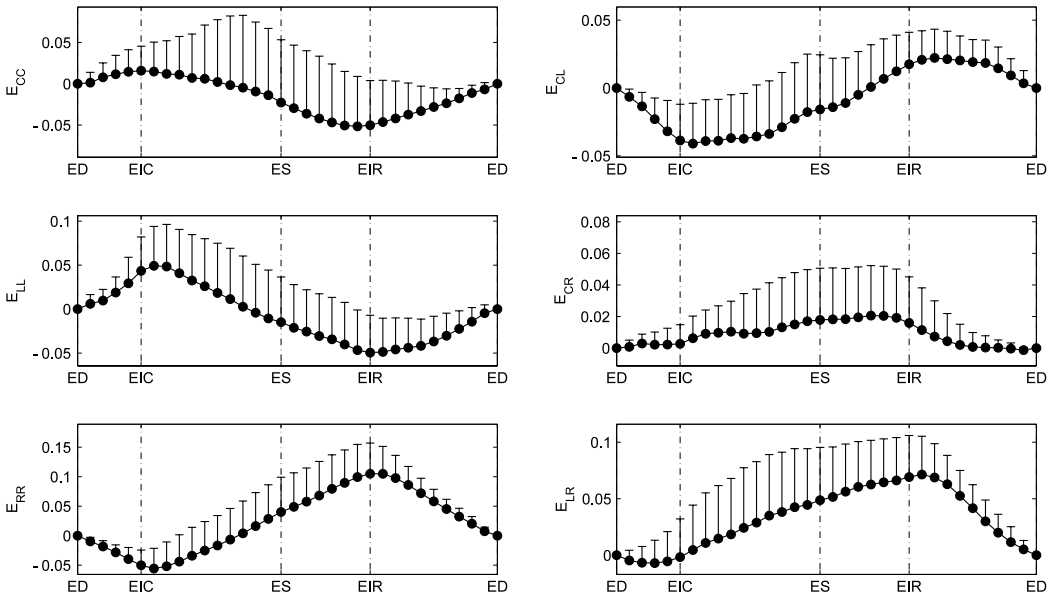

Fig. 5 – Temporal evolution of cardiac strains at 50% depth of the lateral-equatorial left ventricular wall. Maximum circumferential contraction is $-7.9 \pm 3.8\%$ and maximum wall thickening is $+10.5 \pm 5.2\%$. Means and standard deviations of components of the Green–Lagrange strains are displayed for $n = 9$ animals to the top of the curves. C circumferential, R radial, and L longitudinal direction. ED end diastole, EIR end isovolumetric relaxation, ES end systole, and EIC end isovolumetric contraction.

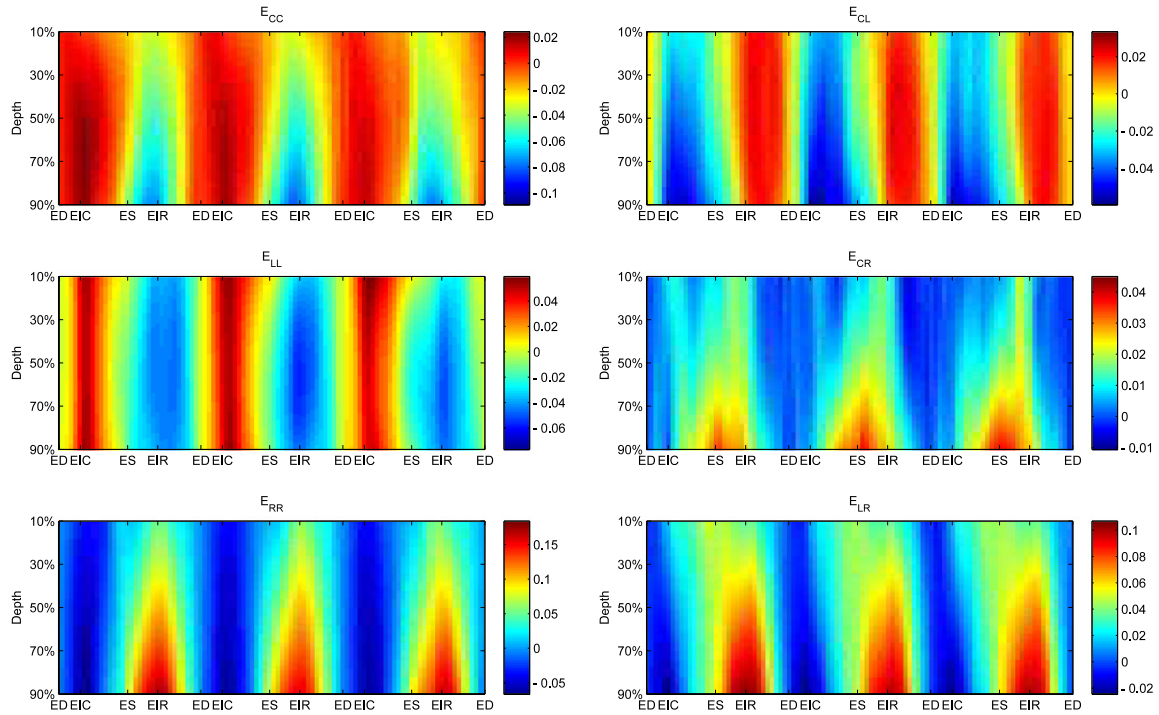

Fig. 6 – Spatio-temporal evolution of cardiac strains in the lateral-equatorial left ventricular wall averaged over $n = 9$ animals. Components of the Green–Lagrange strains are displayed across the ventricular wall with 10% depth indicating the epicardium, the outer wall, and 90% depth indicating the endocardium, the inner wall. Strains are displayed for three consecutive heartbeats. C circumferential, R radial, and L longitudinal direction. ED end diastole, EIR end isovolumetric relaxation, ES end systole, and EIC end isovolumetric contraction.

indicated by the steeper slope in the transition from blue to red. This mechanical excitation pattern closely resembles the electrical excitation pattern starting at the endocardium, progressing gradually outward towards the epicardium, as

the activation wave spreads across the heart (Durrer et al., 1970). This observation is in excellent agreement with the electrophysiological response of endocardial cells, close to the Purkinje fiber system, which display a longer action potential duration than epicardial cells (Göktepe et al., 2010; Kotikanyadanam et al., 2010), meaning they are electrically activated first and deactivated last. Temporal strain variations throughout the cardiac cycle are larger in the endocardium than in the epicardium for both circumferential E_{CC} and radial E_{RR} strains.

4.3. *Spatio-temporal evolution of cardiac strains in the lateral wall*

Fig. 5 displays the temporal evolution of the average cardiac strains at the lateral-equatorial left ventricular midwall, i.e., at 50% depth. For all six strain components, the general trend in the lateral-equatorial wall is similar to the anterior-basal wall, displayed in Fig. 3. There are some minor differences in the circumferential strains E_{CC} at end isovolumetric relaxation, which seem to be less pronounced in the lateral midwall at $-5.1 \pm 6.0\%$ than in the anterior midwall at $-7.9 \pm 3.8\%$. However, the longitudinal extension E_{LL} at end isovolumetric contraction seems to be more pronounced in the lateral midwall at $+4.9 \pm 4.4\%$ than in the anterior midwall at $+0.8 \pm 3.8\%$.

Fig. 6 depicts the spatio-temporal evolution of the average cardiac strains across the lateral-equatorial left ventricular wall, where, again, red indicates positive, i.e., tensile strains, and blue indicates negative, i.e., compressive strains. The general trend seems to be similar to that of the anterior wall, displayed in Fig. 5. Overall, transmural strain variations in the lateral wall seem to be less pronounced than those in the anterior wall, except for the change in the radial strain which is similar to that of the anterior wall. In addition, mechanical activation of the lateral-equatorial wall seems to be *slightly delayed* as compared to that of the anterior-basal wall. This manifests itself in both circumferential E_{CC} and radial E_{RR} strains which are mechanically activated only at end systole. This mechanical activation delay agrees nicely with the electrical activation delay of the lateral-equatorial wall with respect to the anterior-basal wall, which has been reported to be one of the regions of early electrical activation (Durrer et al., 1970).

4.4. *Spatio-temporal evolution of fiber strains in the anterior and lateral wall*

Fig. 7 illustrates the temporal evolution of the average fiber strains E_{FF}, both in the anterior-basal and lateral-equatorial left ventricular wall. The general trends are similar in the anterior and lateral wall. Transmurally, the maximum fiber stretch E_{FF} occurs at end isovolumetric contraction at $+3.5 \pm 4.1\%$ close to the epicardium, decreasing transmurally towards the endocardium, where the maximum fiber stretch E_{FF} is less than $+0.5 \pm 0.9\%$. Transmurally, the maximum fiber contraction E_{FF} occurs between end systole and end isovolumetric relaxation at $-8.0 \pm 2.5\%$ close to the endocardium and in the midwall, decreasing transmurally towards the epicardium, where maximum fiber contraction E_{FF} is only $-6.2 \pm 4.6\%$. Overall, this indicates that fiber strains display a *significant transmural heterogeneity*, being more contractile in the inner wall than in the outer wall and more contractile at the anterior site than at the lateral site. Temporally, maximum fiber contraction is found between end systole and isovolumetric relaxation in the endocardium, progressing across the wall and reaching the epicardium at end isovolumetric relaxation. In this sense, the mechanical activation sequence nicely follows the electrical activation sequence, from endocardium to epicardium, from the anterior-basal to the lateral-equatorial wall, reported in the literature (Durrer et al., 1970). In general, fiber contraction seems to be more pronounced and more coordinated in the anterior-basal than in the lateral-equatorial wall.

Last, Fig. 8 summarizes the spatio-temporal evolution of the average fiber strains E_{FF}, both in the anterior-basal and lateral-equatorial wall. It confirms the general trends observed in Fig. 7. Fiber shortening, represented through blue colors, seems to be more coordinated in the anterior than in the lateral wall. Fiber pre-stretch, indicated through red colors, spans the entire anterior-basal wall and the upper half of the lateral-equatorial wall. Some small pre-stretched regions in the endocardium of the lateral-equatorial wall might be attributed to the tension exerted by the papillary muscles located in this area. Fiber strain profiles are transmurally homogeneous at end diastole, see the almost vertical orange zero-strain lines near end diastole in Fig. 8, top and bottom. This indicates that *fiber relaxation occurs almost simultaneously across the wall* both in the anterior and lateral regions. However, fiber strain profiles are transmurally heterogeneous during systole, see the inclined orange zero-strain lines from end isovolumetric contraction towards end systole in Fig. 8, top and bottom. This indicates that *fiber contraction is initiated at the endocardium* slightly after end diastole *and progresses transmurally outward*, reaching the epicardium slightly before end systole. Fiber relaxation, indicated through the transition from blue to orange, proceeds faster than the fiber contraction, indicated through the transition from orange to blue. Accordingly, *fibers near the outer wall are in contraction for approximately half of the cardiac cycle while fibers near the inner wall are in contraction almost throughout the entire cardiac cycle*. Roughly speaking, in Fig. 8, blue contractile regions with $E_{FF} < 0$ are more pronounced close to the endocardium, while red tensile regions with $E_{FF} > 0$ are more pronounced close to the epicardium. This effect is more pronounced in the anterior-basal than in the lateral-equatorial wall.

5. Discussion

5.1. *Limitations*

A limitation inherent to the proposed marker technique is that it is invasive in nature and therefore not applicable to humans. Although ovine hearts behave relatively similar to human hearts, we need to be careful when extrapolating our findings to cardiac wall dynamics in humans. In fact, the overall goal of this research is to utilize our videofluoroscopic marker technique to validate common non-invasive imaging

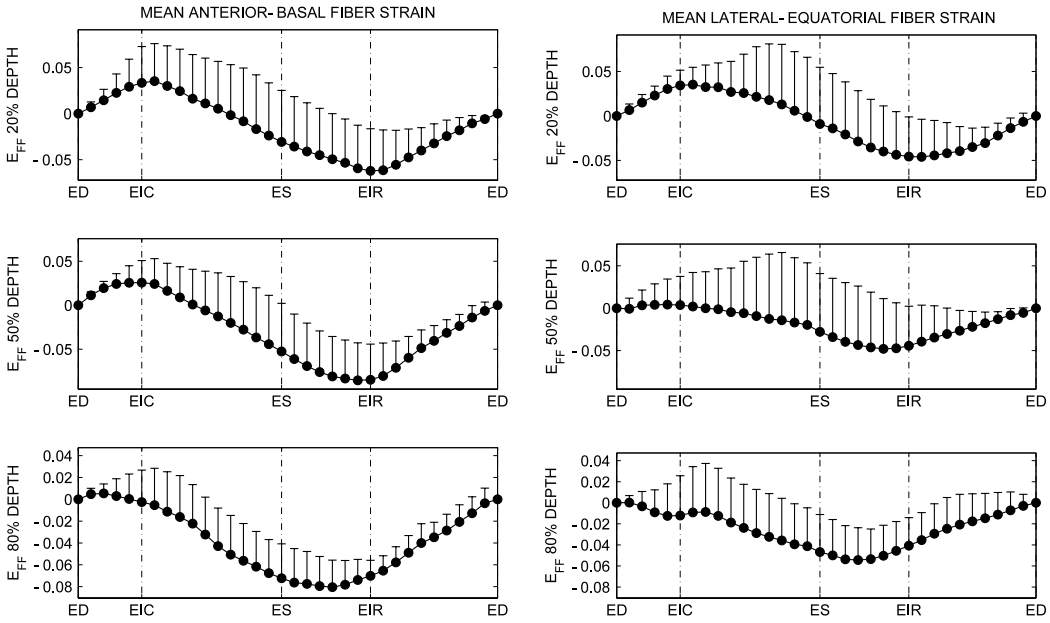

Fig. 7 – Temporal evolution of fiber strains at 20%, 50%, and 80% depth of the anterior-basal and lateral-equatorial left ventricular wall. Maximum fiber contraction varies from $-8.0 \pm 2.5\%$ and $-5.4 \pm 3.1\%$ in the anterior and lateral endocardium, i.e., at 80% depth, to $-6.2 \pm 4.6\%$ and $-4.6 \pm 4.2\%$ in the anterior and lateral epicardium, i.e., at 20% depth. Means and standard deviations are displayed for $n = 9$ animals to the top of the curves. ED end diastole, EIR end isovolumetric relaxation, ES end systole, and EIC end isovolumetric contraction.

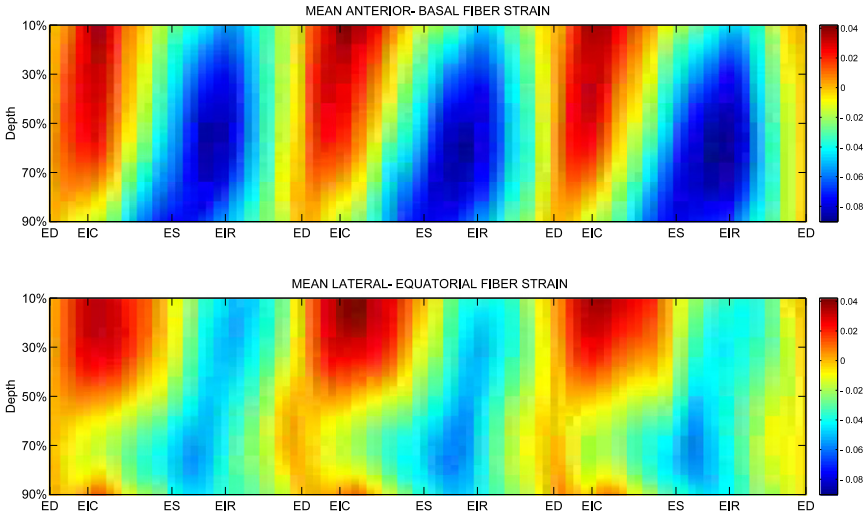

Fig. 8 – Spatio-temporal evolution of fiber strains in the anterior-basal and lateral-equatorial left ventricular wall averaged over $n = 9$ animals. Fiber strains are displayed across the ventricular wall with 10% depth indicating the epicardium, the outer wall, and 90% depth indicating the endocardium, the inner wall. Strains are displayed for three consecutive heartbeats. ED end diastole, EIR end isovolumetric relaxation, ES end systole, and EIC end isovolumetric contraction.

techniques used in human patients in the clinic such as tissue Doppler imaging and speckle tracking echocardiography. Another potential limitation might be that we perform the data acquisition right after the surgical procedure itself. The implantation of myocardial markers and transmural beads is an invasive procedure associated with local left ventricular wall trauma which might potentially lead to acute changes in ventricular wall dynamics. This might explain our relatively low ejection fraction and our relatively low strain values when compared with canine models reported in the literature (Waldman et al., 1985), which, however, agree relatively well with our previous results in ovine models (Cheng et al., 2006a). To quantify these acute effects, we have previously acquired marker and bead coordinates immediately after implantation and several weeks post surgery. While hemodynamics were unfavorably impacted by the surgical intervention, differences in absolute strain values were only minor, and general trends remained unchanged

(Kindberg et al., 2009). Lastly, it could be viewed as a limitation that the results of our computational analysis are sensitive to the chosen reference configuration. After experimenting with different reference configurations, we have chosen end diastole as the strain free reference state. While the choice of the reference state obviously influences the absolute values of the individual strain components, general trends remain unaltered. Different reference configurations basically induce a vertical shift of the strain vs. time curves, but the strain amplitudes remain virtually unchanged. To extract fiber strains, we have used generic fiber orientation maps generated by tissue histology averaged over five animals. It would, of course, be more appropriate to utilize subject-specific fiber orientation maps when projecting the strain tensor onto local fiber directions.

5.2. *Clinical significance*

Left ventricular wall strains and active fiber contraction are believed to be important indicators for left ventricular remodeling. Altered wall strains can result in the production of cytokines and reactive oxygen species stimulating cardiomyocyte apoptosis and extracellular matrix disruption which, in turn, might trigger global left ventricular dilation and remodeling. This study therefore aimed at establishing a baseline characterization of cardiac and fiber strains throughout the cardiac cycle to quantify temporal, regional, and transmural variations of active fiber contraction in the healthy beating heart. Our observed mechanical excitation patterns are in excellent qualitative agreement with the electrical excitation patterns reported in the literature (Durrer et al., 1970). They complement our in vitro database of strains and stresses in healthy cardiac muscle tissue (Böl et al., in press). The identification of deviations from these baseline values is clinically important to guide the optimal timing of clinical interventions, e.g., in asymptomatic severe mitral regurgitation (Carhäll et al., 2008) or in progressive heart failure (Göktepe et al., 2010). The permanent nature of the implanted beadsets renders the proposed marker technology an ideal methodology to quantify chronic kinematic changes during progressive growth and remodeling (Göktepe et al., 2010).

5.3. *Engineering relevance*

The past two decades have seen a clear trend towards patient-specific computational treatment planning in cardiovascular disease. This manuscript has established a baseline characterization of ventricular wall dynamics that might be useful to calibrate and validate mechanistic material models and computational simulation tools for passive cardiac relaxation (Göktepe et al., 2011), active cardiac contraction (Göktepe and Kuhl, 2010), and potential viscous effects (Katsnelson et al., 2004). Lastly, and maybe most importantly, current therapies for heart failure seek to support the ventricular wall to reduce cardiomyocyte overstretch by using synthetic or living tissue engineered solutions (Christman and Lee, 2006). This study provides useful guidelines for the structural and functional requirements of these biomaterials and may therefore be relevant to tissue engineering in general.

6. Conclusions

In summary, this study demonstrates that cardiac wall strains display significant temporal, regional, and transmural variations. Maximum fiber contraction was found to vary from $-8.0 \pm 2.5\%$ and $-5.4 \pm 3.1\%$ in the anterior and lateral endocardium to $-6.2 \pm 4.6\%$ and $-4.6 \pm 4.2\%$ in the anterior and lateral epicardium. Mechanical activation is initiated at the endocardium progressing transmurally outwards towards the epicardium, whereas mechanical deactivation occurs almost simultaneously across the wall. Fibers near the outer wall are therefore in contraction for approximately half of the cardiac cycle while fibers near the inner wall are in contraction almost throughout the entire cardiac cycle. We believe that this work provides a valuable baseline data set to judge strain alterations in response to cardiac disease and treatment, to validate alternative non-invasive imaging modalities, to calibrate and validate material models and computational tools for active cardiac contraction, and to engineer synthetic or living biomaterials with similar structure and function.

Acknowledgments

This work was supported by the US National Institutes of Health grants R01 HL 29589 and R01 HL67025 (Dr. Miller); the US National Science Foundation CAREER award CMMI-0952921 (Dr. Kuhl); the Swiss National Science Foundation Fellowship PBELP2-130913 (Dr. Tsamis); the Western States Affiliate American Heart Association Fellowship (Dr. Swanson); the US–Norway Fulbright Foundation, the Swedish Heart–Lung Foundation, and the Swedish Society for Medical Research (Dr. Kvitting); and the Deutsche Herzstiftung, Frankfurt, Germany, Research Grant S/06/07 (Dr. Bothe).

REFERENCES

Arts, T., Costa, K.D., Covell, J.W., McCulloch, A.D., 2001. Relating myocardial laminar architecture to shear strain and muscle fiber orientation. Am. J. Physiol. Heart Circ. Physiol. 280, H2222–H2229.

Böl, M., Abilez, O.J., Assar, A.N., Zarins, C.K., Kuhl, E., 2011. In vitro / in silico characterization of active and passive stresses in cardiac muscle. Int. J. Multiscale Comput. Eng. (in press).

Böl, M., Reese, S., Parker, K.K., Kuhl, E., 2009. Computational modeling of muscular thin films for cardiac repair. Comput. Mech. 43, 535–544.

Carhäll, C., Nguyen, T.C., Itoh, A., Ennis, D.B., Bothe, W., Liang, D., Ingels, N.B., Miller, D.C., 2008. Alterations in transmural myocardial strain: an early marker of left ventricular dysfunction in mitral regurgitaiton? Circulation 118, S256–S262.

Cheng, A., Langer, F., Rodriguez, F., Criscione, J.C., Daughters, G.T., Miller, D.C., Ingels, N.B., 2005a. Transmural cardiac strains in the lateral wall of the ovine left ventricle. Am. J. Physiol. Heart Circ. Physiol. 288, H1546–H1556.

Cheng, A., Langer, F., Rodriguez, F., Criscione, J.C., Daughters, G.T., Miller, D.C., Ingels, N.B., 2005b. Transmural sheet strains in the lateral wall of the ovine left ventricle. Am. J. Physiol. Heart Circ. Physiol. 289, H1234–H1241.

Cheng, A., Nguyen, T.C., Malinowski, M., Daughters, G.T., Miller, D.C., Ingels, N.B., 2008. Heterogeneity of left ventricular wall thickening mechanisms. Circulation 118, 713–721.

Cheng, A., Nguyen, T.C., Malinowski, M., Ennis, D.B., Daughters, G.T., Miller, D.C., Ingels, N.B., 2006a. Transmural left ventricular shear strain alterations adjacent to and remote from infarcted myocardium. J. Heart Valve Dis. 15, 209–218.

Cheng, A., Nguyen, T.C., Malinowski, M., Langer, F., Liang, D., Daughters, G.T., Ingels, N.B., Miller, D.C., 2006b. Passive ventricular constraint prevents transmural shear strain progression in left ventricle remodeling. Circulation 114, I79–I86.

Christman, K.L., Lee, R.J., 2006. Biomaterials for the treatment of myocardial infarction. J. Am. Coll. Cardiol. 48, 907–913.

Coppola, B.A., Covell, J.W., McCulloch, A.D., Omens, J.H., 2007. Asynchrony of ventricular activation affects magnitude and timing of fiber stretch in late-activated regions of the canine heart. Am. J. Physiol. Heart Circ. Physiol. 293, H754–H761.

Costa, K.D., Takayama, Y., McCulloch, A.D., Covell, J.W., 1999. Laminar fiber architecture and three-dimensional systolic mechancis in canine ventricular myocardium. Am. J. Physiol. Heart Circ. Physiol. 276, 595–607.

Daughters, G.T., Sanders, W.J., Miller, D.C., Schwarzkopf, A., Mead, C.W., Ingels, N.B., 1989. A comparison of two analytical systems for 3-D reconstruction from biplane videograms. Proc. of IEEE Comput. Cardiol. 15, 79–82.

Durrer, D., van Dam, R.T., Freud, G.E., Janse, M.J., Meijler, F.L., Arzbaecher, R.C., 1970. Total excitation of the isolated human heart. Circulation 41, 899–912.

Ennis, D.B., Nguyen, T.C., Riboh, J.C., Wingström, L., Harrington, K.B., Daughters, G.T., Ingels, N.B., Miller, D.C., 2008. Myofiber angle distributions in the ovine left ventricle do not conform to computationally optimized predictions. J. Biomech. Eng. 41, 3219–3224.

Fenton, T.R., Cherry, J.M., Klassen, G.A., 1978. Transmural myocardial deformation in the canine left ventricular wall. Am. J. Physiol. 235, H523–H530.

Gaudron, P., Eilles, C., Kubler, I., Ertl, G., 1993. Progressive left ventricular dysfunction and remodeling after myocardial infarction. Circulation 87, 755–763.

Göktepe, S., Abilez, O.J., Kuhl, E., 2010. A generic approach towards finite growth with examples of athlete's heart, cardiac dilation, and cardiac wall thickening. J. Mech. Phys. Solids 58, 1661–1680.

Göktepe, S., Abilez, O.J., Parker, K.K., Kuhl, E., 2010. A multiscale model for eccentric and concentric cardiac growth through sarcomerogenesis. J. Theoret. Biol. 265, 433–442.

Göktepe, S., Acharya, S.N.S., Wong, J., Kuhl, E., 2011. Computational modeling of passive myocardium. Int. J. Numer. Methods Biomed. Eng. 27, 1–12.

Göktepe, S., Kuhl, E., 2010. Electromechanics of cardiac tissue: a unified approach to the fully coupled excitation-contraction problem. Comput. Mech. 45, 227–243.

Göktepe, S., Wong, J., Kuhl, E., 2010. Atrial and ventricular fibrillation—computational simulation of spiral waves in cardiac tissue. Arch. Appl. Mech. 80, 569–580.

Katsnelson, L.B., Nikitina, L.V., Chemla, D., Solovyova, O., Coirault, C., Lecarpentier, Y., Markhasin, V.S., 2004. Influence of viscosity on myocardial mechanical activity: a mathematical model. J. Theoret. Biol. 230, 385–405.

Kindberg, K., Carhäll, C., Karlsson, M., Nguyen, T.C., Cheng, A., Langer, F., Rodriguez, F., Daughters, G.T., Miller, D.C., Ingels, N.B., 2007. Transmural strains in the ovine left ventricular lateral wall during diastolic filling. J. Biomech. Eng. 131, 061004-1–061004-8.

Kindberg, K., Karlsson, M., Ingels, N.B., Criscione, J.C., 2009. Nonhomogeneous strain from sparse marker arrays for analysis of transmural myocardial mechanics. J. Biomech. Eng. 129, 603–610.

Kotikanyadanam, M., Göktepe, S., Kuhl, E., 2010. Computational modeling of electrocardiograms—a finite element approach towards cardiac excitation. Int. J. Numer. Methods Biomed. Eng. 26, 524–533.

Leong, K.F., Chua, C.K., Sudarmadji, N., Yeong, W.Y., 2008. Engineering functionally graded tissue engineering scaffolds. J. Mech. Behav. Biomed. Mater. 1, 14–152.

Lloyd-Jones, D., Adams, R.J., Brown, T.M., Carnethon, M., Dai, S., De Simone, G., Ferguson, T.B., Ford, E., Furie, K., Gillespie, C., Go, A., Greenlund, K., Haase, N., Hailpern, S., Ho, P.M., Howard, V., Kissela, B., Kittner, S., Lackland, D., Lisabeth, L., Marelli, A., McDermott, M.M., Meigs, J., Mozaffarian, D., Mussolino, M., Nichol, G., Roger, V.L., Rosamond, W., Sacco, R., Sorlie, P., Stafford, R., Thom, T., Wasserthiel-Smoller, S., Wong, N.D., Wylie-Rosett, J., 2010. Heart disease and stroke statistics—2010 Update. A report fromt eh American heart association. Circulation 121, e46–e215.

McCulloch, A.D., Omens, J.H., 1991. Non-homogeneous analysis of three-dimensional transmural finite deformation in canine ventricular myocardium. J. Biomech. 24, 539–548.

McGee, E.C., Gillinov, A.M., McCarthy, P.M., 2006. Reverse ventricular remodeling: mechanical options. Curr. Opin. Cardiol. 21, 215–220.

Niczyporuk, M.A., Miller, D.C., 1991. Automatic tracking and digitization of multiple radiopaque myocardial markers. Comput. Biomed. Res. 24, 129–142.

Rausch, M.K., Bothe, W., Kvitting, J.P., Göktepe, S., Miller, D.C., Kuhl, E., 2011. In vivo dynamic strains of the ovine anterior mitral valve leaflet. J. Biomech. 44, 1149–1157.

Rausch, M.K., Bothe, W., Kvitting, J.P., Swanson, J.C., Ingels, N.B., Miller, D.C., Kuhl, E., Characterization of mitral valve annular dynamics in the beating heart. Ann. Biomed Eng. in press (doi:10.1007/s10439-011-0272-y).

Takayama, Y., Costa, K.D., Covell, J.W., 2002. Contribution of laminar myofiber architecture to load-dependent changes in mechanics of LV myocardium. Am. J. Physiol. Heart Circ. Physiol. 282, H1510–H1520.

Waldman, L.K., Fung, Y.C., Covell, J.W., 1985. Transmural muocardial deformation in the canine left ventricle. Normal in vivo three-dimensional finite strains. Circ. Res. 57, 152–163.

Wollert, K.C., Meyer, G.P., Lotz, J., Ringes-Lichtenberg, S., Lippolt, P., Breidenbach, C., Fichtner, S., Korte, T., Hornig, B., Messinger, D., Arseniev, L., Hertenstein, B., Ganser, A., Drexler, H., 2004. Intracoronary autologous bone-marrow cell transfer after myocardial infarction: the BOOST randomised controlled clinical trial. Lancet 364, 141–148.